Petroleum Science 23 (2026) 777–790

Contents lists available at ScienceDirect

Petroleum Science

journal homepage: www.keaipublishing.com/en/journals/petroleum-science

Original Paper

Study on the phase behavior and minimum miscible pressure of CO_2-shale oil in nanopores with confinement effect

Ying Xiong [a,b,*], Peng-Fei Chen [a,b], Wan-Fen Pu [c], Rui Jiang [a], Qin Pang [c]

[a] Research Institute of Natural Gas Technology, PetroChina Southwest Oil & Gas Field Company, Chengdu, 610500, Sichuan, China
[b] Shale Gas Geological Evaluation and Efficient Exploitation Key Laboratory of Sichuan Province, Chengdu, 610213, Sichuan, China
[c] State Key Laboratory of Oil and Gas Reservoir Geology and Exploitation, Southwest Petroleum University, Chengdu, 610500, Sichuan, China

ARTICLE INFO

Article history:
Received 18 April 2025
Received in revised form
17 November 2025
Accepted 19 November 2025
Available online 25 November 2025

Edited by Jia-Jia Fei

Keywords:
Nano-confinement effect
Phase equilibrium calculation
Minimum miscible pressure
Vanishing interfacial tension
CO_2-EOR

ABSTRACT

CO_2 injection is a significant enhanced oil recovery method in shale oil reservoirs and facilitates the mitigation of CO_2 emissions. However, the phase behavior and miscibility process of light shale oil and CO_2 system in shale reservoirs with widely distributed nanopores remain uncertain. Based on the thermodynamic equilibrium theory and the modified Peng-Robinson equation of state (PR-EOS), a confined fluid model considering the effect of nanoconfinement (critical property shift and adsorption) and capillarity was used to study the phase diagram and thermodynamic property of shale oil-CO_2 mixtures. The validity of the fluid model in bulk and in nanopores was verified with the pressure-volume-temperature (PVT) experiments and literature data, respectively. The interfacial tension (IFT) and minimum miscible pressure (MMP) were determined by the Parachor model and IFT vanishing method (VIT), respectively. The effects of pore sizes, temperature and injected gas type and compositions on the IFT and MMP was comprehensively investigated. The result shows that the nanoconfinement effect causes the two-phase region in the phase diagram of reservoir fluids to contract and enhances the ability of CO_2 and light components to enter smaller pores, thus reducing the bubble point pressure, oil density, oil viscosity and IFT of shale oil-CO_2 mixtures in nanopores. The nanoconfinement effect is more pronounced in pore radius of less than 50 nm, with roughly 16% reduction in the MMP of shale oil-CO_2 mixtures. Temperature has a negative effect on the IFT and MMP of shale oil-CO_2 mixtures due to the decreased solubility of CO_2 under high temperature. The miscibility of CO_2 and shale oil is improved by propane (C_3H_8) and ethane (C_2H_6), while decreased by methane (CH_4).

1. Introduction

With global energy demand continuing to increase, unconventional oil resources such as tight oil and shale oil have received widespread attention (Ju et al., 2019; Lee et al., 2020; Pang et al., 2024). It was estimated that the total shale oil reserves in the world reached to 6.9 trillion barrels, with oil production constituting roughly 10% of total global crude oil output (Jin et al., 2021). Shale reservoirs are typically characterized with widely distributed nanoscale pores and some reported macroscale natural fractures (Huang and Zhao, 2023; Wang D. et al., 2024). The multiscale pore structure of shale reservoirs leads to unique phase behavior and thermodynamic properties that deviates from the bulk conditions (Dong et al., 2016; Pitakbunkate et al., 2016; Zhang et al., 2019b). Therefore, a comprehensive understanding of the phase behavior and thermodynamic properties of reservoir fluids in shale nanopores is essential for efficient development of shale oils.

The deviations of phase behavior and thermodynamic properties are primarily attributed to nano-confinement effect, which intensify due to strong solid-fluid interactions especially when the pore dimensions become comparable to fluid molecule sizes (Li et al., 2024; Song et al., 2020; Vishnyakov et al., 2001). In recent years, a number of experimental, theoretical and molecular simulation methods have been employed to investigate the fluid phase behavior and thermodynamic property in nanoscale pores (Song et al., 2024a; Sun et al., 2023; Wang Y. et al., 2024). Experimental method refers to direct/indirect measurement of fluid thermodynamic parameters to determine fluid phase transition

* Corresponding author.
E-mail address: xiong_y@petrochina.com.cn (Y. Xiong).
Peer review under the responsibility of China University of Petroleum (Beijing).

https://doi.org/10.1016/j.petsci.2025.11.039

process, which mainly includes adsorption-desorption method (Liu and Zhang, 2019), differential scanning calorimetry (DSC) method (Luo et al., 2016) and nanofluidic method (Bao et al., 2021; Nguyen et al., 2015). Molecular simulations can provide microscale insights into the surface-molecule interactions and calculate fluid thermodynamic parameters (Wang et al., 2021; Zhou et al., 2016). A key consensus has been reached that the critical temperature and pressure of fluid component are suppressed in nanopores, while the fluid density near pore surfaces significantly exceeds that in pore centers, indicating the adsorption effect and capillary pressure in nanopores is unneglectable (Tan et al., 2019; Tian et al., 2021). However, both experimental process and molecular simulation methods are time-consuming. Based on the experimental and molecular simulation results, theoretical model incorporating nanoconfinement effects is promising as it offers computationally efficient approaches for exploring large amounts of fluid thermodynamic and phase behavior parameters within nanopores. Song et al. (2024a, 2020) proposed a modified PR-EOS accounting for critical property shift, adsorption and capillarity and performed multiple phase equilibrium calculations of CO_2-shale oil mixtures considering the multi-scale distribution of shale nanopores. Therefore, incorporating the nano-confinement effect into classical equation of state equation (EOS) is crucial to mimic fluid phase behavior within nanopores.

Minimum miscible pressure (MMP) is the threshold pressure for dynamic miscibility between CO_2 and crude oil at any ratios, which is crucial for determining the efficiency of CO_2-EOR in shale reservoirs (Adekunle and Hoffman, 2016). When CO_2 is injected into typical shale reservoirs, it changes to supercritical phases and leads to oil volume expansion, reduced oil viscosity and interfacial tension (IFT) through dissolution and extraction mechanisms (Seyyedsar et al., 2016). Numerous methods have been proposed to determine the MMP of multicomponent mixtures (Adekunle and Hoffman, 2016; Ahmadi and Johns, 2011; Iraji et al., 2015). Experimental approaches mainly include slim-tube method, rising bubble apparatus (RBA), and vanish interfacial tension (VIT) methods. However, slim-tube method is highly time-consuming despite its accuracy, while RBA has been reported less efficient for condensing gas drive. VIT method based on the principle of zero interfacial tension at miscible gas and oil interface is efficient and reliable for MMP determination (Cao and Gu, 2013; Rao, 1997). Recently, microfluidic model has been employed with direct visual observation of the vanishing interface of CO_2 and oil, which achieves the maximum deviation of only 3.83% from literature reported values (Shi et al., 2024). Molecular dynamic simulations have revealed that the nano-confinement effect reduces the MMP compared to bulk phase conditions due to strong fluid-solid interactions (Sun et al., 2023). However, in the common practice of molecular simulations, the shale nanopores are oversimplified as carbon nanotubes or graphene slits, and shale oil as pure alkanes or alkane mixtures (Li et al., 2019; Yang et al., 2020). Therefore, the accuracy and efficiency of simple modelling for MMP determination remains to be researched. Consequently, theoretical estimation of MMP based on the modified EOS incorporating nano-confinement effect and VIT method to extrapolate the IFT-pressure curves to zero values has attracted growing attention (Ashrafizadeh and Ameri Ghasrodashti, 2011; Sun et al., 2024).

In this study, a confined fluid model incorporating nano-confinement effect (critical property shift and adsorption) and capillarity was applied to determine the phase behavior and MMP of shale oil-CO_2 system. Based on the thermodynamic equilibrium theory and the modified PR-EOS, the phase behavior and thermodynamic property of CO_2 and the shale oil from the Sichuan Basin, China in nanopores was investigated. The validity of the confined fluid model both in bulk and in nanopores has been confirmed, using the pressure-volume-temperature (PVT) experiment conducted in this work and the experimental results taken from the literature. Subsequently, the effects of pore sizes, temperature and injected gas type and compositions on the IFT and MMP was investigated.

2. Experimental

2.1. Materials

In this study, the shale oil sample was collected from the Da'anzhai Formation in Sichuan Basin, China, which lies 3150 m underneath. Table 1 presents the detailed shale oil properties. The stock oil density is 0.8174 g/cm^3 and the viscosity is 3.55 mPa·s. The content of saturates, aromatics, resins and asphaltenes is 61.8%, 29.5%, 7.8% and 0.8%, respectively. Under the formation condition (340.15 K, 40 MPa), the dissolved gas-oil ratio (GOR) of shale oil is 122.82 m^3/m^3 and the saturation pressure (P_b) is 20.88 MPa. The crude oil expansion coefficient (B_o) is 1.35. Gaseous solvent CO_2 has the purity of 99.998 mol% (Kelong Chemicals Agency, Chengdu). Subsequently, PVT experiments were carried out to calibrate shale oil model at bulk phase.

2.2. PVT experiment

Fig. 1 shows a simplified schematic diagram of PVT experimental setup. A mercury-free DBR PVT system (Schlumberger) which has a maximum pressure of 70 MPa and maximum temperature of 473.15 K is used to perform constant composition expansion (CCE) and swelling test (ST) experiments.

In this work, CCE tests were conducted at reservoir temperature to establish the relationship between pressure and fluid volume for the fluids. Initially, nearly 100 cm^3 of single-phase shale oil fluids were loaded to the PVT cell and then heated to 340.15 K. The initial volume of single-phase fluids was measured at initial pressure (P_{ini}). Subsequently, the pressure was reduced gradually until it reached a prescribed value. Notably, the pressure reduction was 5 MPa before and 3 MPa after visually observed evident gas expansion in the cell. During the pressure decline process, no fluids were removed from the PVT cell and the fluid composition remains unchanged. The total volume of fluids at each pressure point was repeatedly measured. Therefore, the pressure-volume relationship was obtained and the initial saturation pressure (P_b) or bubble point pressure was determined by linearly extrapolating the two phases of the *P-V* relationship data. The relative volume (ROV) is defined as the ratio of the total fluid volume at given pressure to the total fluid volume at P_b.

ST was performed at different CO_2 concentrations to evaluate the capacity of gas dissolution and oil expansion. Typically, nearly 100 cm^3 of single-phase shale oil were loaded to the PVT cell and then heated to 340.15 K. A known volume of CO_2 solvent was injected into the PVT cell and stirred with shale oils to facilitate gas dissolution. Subsequently, the volume of single-phase oil-gas mixtures was recorded at P_{ini} and new saturation pressure (P_{sat}) was determined by repeating pressure declining process as in the

Table 1
Summary of shale oil properties.

Property	Value	Property	Value
Saturates, %	61.8	Stock oil density, g/cm^3	0.8174
Aromatics, %	29.5	Stock oil viscosity, mPa·s	3.55
Resins, %	7.8	Saturation pressure (P_b), MPa	20.88
Asphaltenes, %	0.8	GOR at P_b, m^3/m^3	122.82
Molecular weight, g/mol	168.08	B_o at P_b, m^3/m^3	1.35

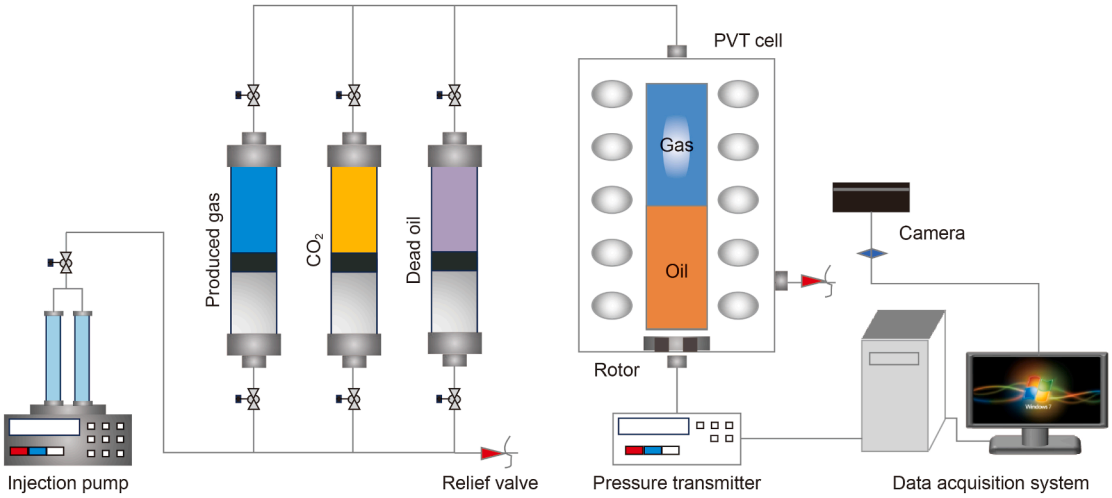

Fig. 1. Schematic illustration of PVT experiment setup.

CCE test. The oil swelling factor (SF) is defined as the ratio of the volume of oil-gas mixtures at each P_{sat} to the shale oil volume at P_b. It should be noted that the PVT experimental results were used to adjust the critical parameters and binary coefficients of PR-EOS for shale oil components.

2.3. Compositional fitting of PVT data

To accurately characterize the shale oil and reduce computational time, the shale oil components was determined by GC and lumped into eight pseudo-components, as listed in Table 2. Notably, the measured oil properties and CO_2-shale oil interactions remains unaffected by the lumping process (Shen and Sheng, 2018). After lumping process, multiple regression analyses were performed to match the calculated PVT data with the measured PVT data, thereby obtaining the tuned EOS parameters. The main tuned parameters include the critical pressure (P_{cb}), critical temperature (T_{cb}), critical volume (V_c), acentric factor (ω), parachor number (ξ) and molecular weight (M_w) of heavy hydrocarbon components, as well as binary coefficient between CO_2 and other components (k_{ij}). The tuned critical parameters and binary coefficients were used in the bulk fluid model, and the confined fluid model was refined by incorporating nanoconfinement effect, which will be discussed below.

Fig. 2 shows the measured and calculated results of CCE and ST experiments. As shown in Fig. 2(a), ROV rapidly increases with decreasing pressure after saturation pressure, which indicates a rapid gas release from liquid phase. The saturation pressure obtained by simulation is 19.98 MPa, and the relative error with the measured value (20.88 MPa) is 4.49%. Fig. 2(b) shows that the measured P_{sat} and SF increase as CO_2 concentrations increases due to CO_2 dissolution. When CO_2 concentration increases to 59 mol%, the P_{sat} rises to 39.05 MPa and the SF increases to 1.51, indicating that CO_2 has a significant effect in expanding oil volume. Fig. 2(c) and (d) shows that the calculated relative error of SF and P_{sat} is below 5%, which indicates that high agreement between experimental results and calculations was obtained. Tables 2 and 3 present the tuned EOS critical parameters and binary interaction coefficients for each component obtained after fitting process.

3. Methodology

3.1. Confinement effect in nanopores

Shale nanopores are widely distributed in the range of 5–20 nm (Zheng et al., 2022), where molecule-surface interactions dominate over molecule-molecule interactions. As shown in Fig. 3, fluid molecules preferentially adsorb on the pore surfaces, which leads to the formation of adsorbed layer. The adsorbed layer becomes increasingly significant as pore size decreases due to the limited total number of fluid molecules in smaller pores, which leads to the restrictions of fluid molecules transports.

As assessing hydrocarbons adsorption in nanopores are usually time-consuming and costly, here we adopt an empirical correlation to calculate the thickness of adsorption layer (Liongseng et al., 1966; Zhang et al., 2019b),

$$\delta_{ad} = \frac{\alpha}{\ln(r_p/\sigma_{LJ})} + \beta\left(\frac{\sigma_{LJ}}{r_p}\right) \tag{1}$$

$$\alpha = -8.3140 \times 10^{-14} M_w{}^2 + 2.0475 \times 10^{-11} M_w + 3.0886 \times 10^{-11} \tag{2}$$

Table 2
Critical properties for shale oil components.

Component	z	P_{cb}, MPa	T_{cb}, K	V_c, L/mol	M_w, g/mol	ω	ξ
CO_2	0.00061	7.37	304.2	0.094	44.01	0.225	78
C_1	0.40843	4.60	190.6	0.099	16.043	0.008	77
C_2	0.05826	4.88	305.4	0.148	30.07	0.098	108
C_3	0.03059	4.24	369.8	0.203	44.097	0.152	150.3
C_4–C_6	0.05546	3.44	474.109	0.3085	74.578	0.242	227.302
C_7–C_{12}	0.26424	2.25	595.919	0.377	121.082	0.322	346.523
C_{13}–C_{21}	0.13133	2.21	783.96	0.997	222.061	0.826	594.440
C_{22}–C_{36}	0.05108	1.45	1007.4	1.246	346.025	1.180	839.553

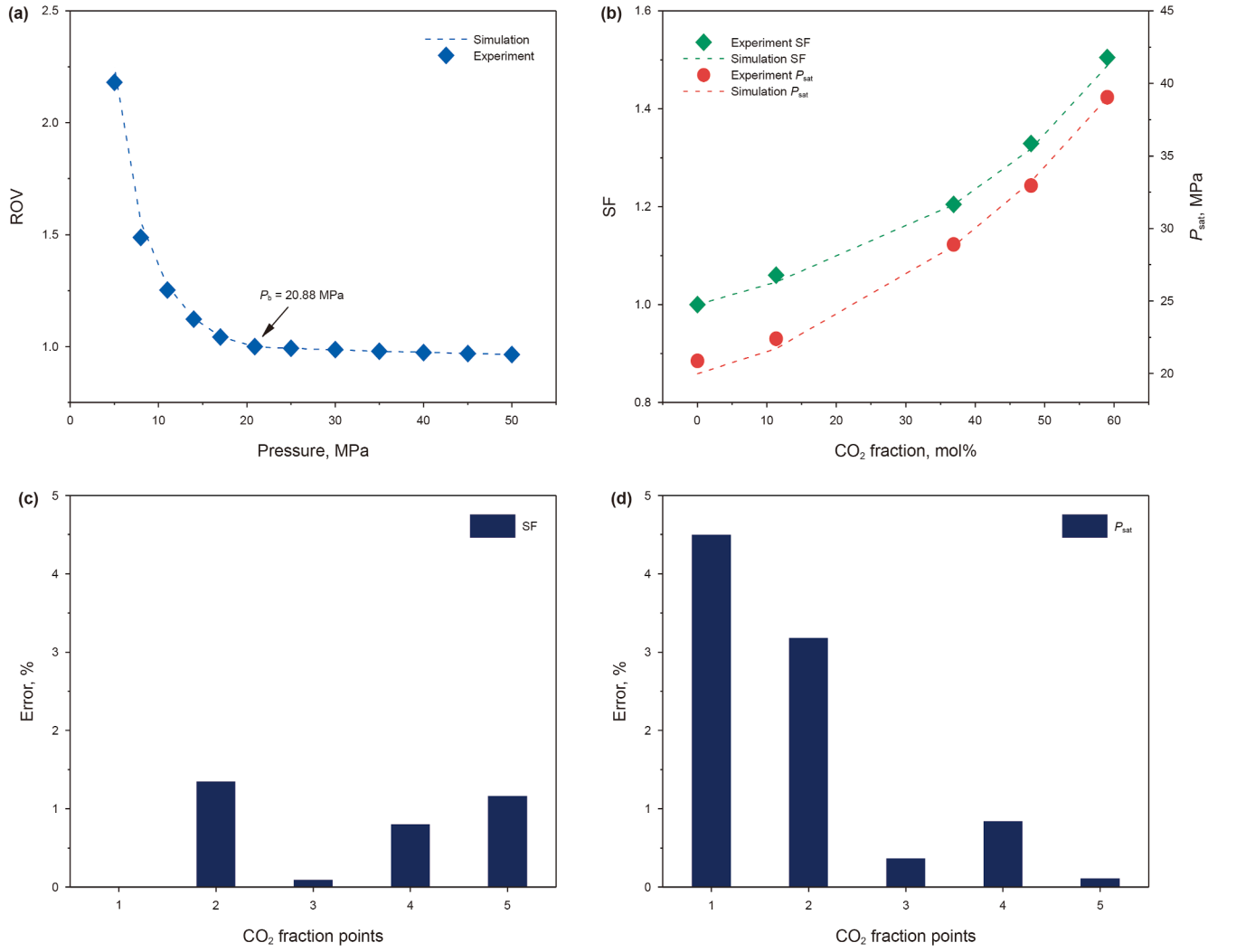

Fig. 2. Comparison of PVT data between experiment and simulation: (**a**) ROV, (**b**) SF and P_{sat}, and relative errors of SF (**c**) and P_{sat} (**d**).

Table 3
Binary interaction coefficients for shale oil components.

Component	CO_2	C_1	C_2	C_3	C_4–C_6	C_7–C_{12}	C_{13}–C_{21}	C_{22}–C_{36}
CO_2	0	0	0.1148	0.125	0.2	0.2	0.111	0
C_1	0	0	0.0012	0.0039	0.0099	0.0137	0.0396	0.0472
C_2	0.1148	0.0012	0	0.0007	0.0041	0.0067	0.0274	0.0339
C_3	0.125	0.0039	0.0007	0	0.0013	0.0029	0.0192	0.0248
C_4–C_6	0.2	0.0099	0.0041	0.0013	0	0.0003	0.0105	0.0148
C_7–C_{12}	0.2	0.0137	0.0067	0.0029	0.0003	0	0.0072	0.0109
C_{13}–C_{21}	0.111	0.0396	0.0274	0.0192	0.0105	0.0072	0	0.0003
C_{22}–C_{36}	0	0.0472	0.0339	0.0248	0.0148	0.0109	0.0003	0

$$\beta = -6.3565 \times 10^{-14} M_w^{\,2} + 3.1550 \times 10^{-11} M_w - 5.8538 \times 10^{-10} \tag{3}$$

$$\sigma_{LJ} = 0.244 \sqrt[3]{\frac{T_{cb}}{P_{cb}}} \tag{4}$$

where δ_{ad} is the adsorption layer thickness; α and β are related coefficients; T_{cb} and P_{cb} are the initial critical temperature and pressure of component i at bulk phase, which are obtained from the compositional fitted PVT data (as shown in Table 2); σ_{LJ} denotes the Lennard-Jones collision diameter; M_w is the molecular weight; r_p refers to the shale nanopore radius. Critical property shifts changing with decreasing pore radius is expressed as (Sun and Li, 2021; Zarragoicoechea and Kuz, 2004),

$$T_c = T_{cb}\left[1 - 0.9409\frac{\sigma_{LJ}}{r_p - \delta_{ad}} + 0.2415\left(\frac{\sigma_{LJ}}{r_p - \delta_{ad}}\right)^2\right] \tag{5}$$

$$P_c = P_{cb}\left[1 - 0.9409\frac{\sigma_{LJ}}{r_p - \delta_{ad}} + 0.2415\left(\frac{\sigma_{LJ}}{r_p - \delta_{ad}}\right)^2\right] \tag{6}$$

where T_c and P_c are the critical temperature and pressure of component i in nanopores.

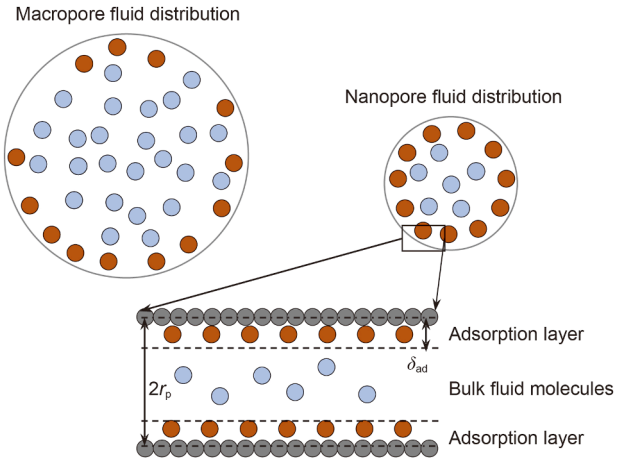

Fig. 3. Fluid molecules distribution in macro and nanopores.

3.2. Peng-Robinson equation of state

PR-EOS (Ashrafizadeh and Ameri Ghasrodashti, 2011) is used to calculate the fugacity for vapor and liquid phase, as described in Eq. (7),

$$P=\frac{RT}{V-b_{\mathrm{m}}}-\frac{a_{\mathrm{m}}}{V(V+b_{\mathrm{m}})+b_{\mathrm{m}}(V-b_{\mathrm{m}})} \tag{7}$$

where the parameters a_{m} and b_{m} for respective vapor and liquid phase are estimated using the van der Waals mixing rule,

$$a_{\mathrm{mL}}(T)=\sum_{i=1}^{nc}\sum_{j=1}^{nc}x_i x_j\left(a_i a_j \alpha_i \alpha_j\right)^{0.5}\left(1-k_{ij}\right) \tag{8}$$

$$a_{\mathrm{mV}}(T)=\sum_{i=1}^{nc}\sum_{j=1}^{nc}y_i y_j\left(a_i a_j \alpha_i \alpha_j\right)^{0.5}\left(1-k_{ij}\right) \tag{9}$$

$$b_{\mathrm{mL}}=\sum_{i=1}^{nc}x_i b_i \tag{10}$$

$$b_{\mathrm{mV}}=\sum_{i=1}^{nc}y_i b_i \tag{11}$$

where $A_{\mathrm{V}}=\frac{a_{\mathrm{mV}}P_{\mathrm{V}}}{(RT)^2}$, $A_{\mathrm{L}}=\frac{a_{\mathrm{mL}}P_{\mathrm{L}}}{(RT)^2}$, $B_{\mathrm{V}}=\frac{b_{\mathrm{mV}}P_{\mathrm{V}}}{RT}$, $B_{\mathrm{L}}=\frac{b_{\mathrm{mL}}P_{\mathrm{L}}}{RT}$, Z_{V} and Z_{L} refer to the compressibility factors for vapor and liquid phase, respectively. The fugacity coefficients for vapor and liquid phase are,

$$\begin{aligned}\ln\phi_{\mathrm{V},i}=&\frac{b_i}{b_{\mathrm{mV}}}(Z_{\mathrm{V}}-1)-\ln(Z_{\mathrm{V}}-B_{\mathrm{V}})\\&-\frac{A_{\mathrm{V}}}{2\sqrt{2}B_{\mathrm{V}}}\left(\frac{2\psi_{\mathrm{V},i}}{a_{\mathrm{mV}}}-\frac{b_i}{b_{\mathrm{mV}}}\right)\ln\left(\frac{Z_{\mathrm{V}}+2.414B_{\mathrm{V}}}{Z_{\mathrm{V}}-0.414B_{\mathrm{V}}}\right)\end{aligned} \tag{12}$$

$$\begin{aligned}\ln\phi_{\mathrm{L},i}=&\frac{b_i}{b_{\mathrm{mL}}}(Z_{\mathrm{L}}-1)-\ln(Z_{\mathrm{L}}-B_{\mathrm{L}})\\&-\frac{A_{\mathrm{L}}}{2\sqrt{2}B_{\mathrm{L}}}\left(\frac{2\psi_{\mathrm{L},i}}{a_{\mathrm{mL}}}-\frac{b_i}{b_{\mathrm{mL}}}\right)\ln\left(\frac{Z_{\mathrm{L}}+2.414B_{\mathrm{L}}}{Z_{\mathrm{L}}-0.414B_{\mathrm{L}}}\right)\end{aligned} \tag{13}$$

where k_{ij} is the binary interaction coefficient (as shown in Table 3), $\psi_{\mathrm{V},i}=\sum_{j=0}^{nc}y_j\left(a_i a_j \alpha_i \alpha_j\right)^{0.5}\left(1-k_{ij}\right)$, and $\psi_{\mathrm{L},i}=\sum_{j=0}^{nc}x_j\left(a_i a_j \alpha_i \alpha_j\right)^{0.5}\left(1-k_{ij}\right)$.

3.3. Vapor and liquid equilibrium calculation

According to the thermodynamic theory, the fugacity of vapor and liquid phases accounting for capillarity in nanopores are,

$$f_{\mathrm{L},i}=x_i\phi_{\mathrm{L},i}P_{\mathrm{L}} \tag{14}$$

$$f_{\mathrm{V},i}=y_i\phi_{\mathrm{V},i}P_{\mathrm{V}}=y_i\phi_{\mathrm{V},i}\left(P_{\mathrm{L}}+P_{\mathrm{cap}}\right) \tag{15}$$

where $f_{\mathrm{V},i}$ and $f_{\mathrm{L},i}$ are the fugacity of component i in vapor and liquid phase, respectively; $\phi_{\mathrm{V},i}$ and $\phi_{\mathrm{L},i}$ are the fugacity coefficient of component i in vapor and liquid phase, respectively; y_i and x_i are the mole fraction of component i in vapor and liquid phase, respectively; P_{V} and P_{L} are the pressure of vapor and liquid phase, respectively; P_{cap} is the capillary pressure. At vapor-liquid phase equilibrium conditions, there exists:

$$\ln f_{\mathrm{V},i}-\ln f_{\mathrm{L},i}=0 \tag{16}$$

The phase equilibrium constant is defined as,

$$K_i=\frac{y_i}{x_i}=\frac{\phi_{\mathrm{L},i}P_{\mathrm{L}}}{\phi_{\mathrm{V},i}P_{\mathrm{V}}}=\frac{\phi_{\mathrm{L},i}P_{\mathrm{L}}}{\phi_{\mathrm{V},i}\left(P_{\mathrm{L}}+P_{\mathrm{cap}}\right)} \tag{17}$$

The value of K_i is calculated by the Rachford-Rice equation (Wei et al., 2022),

$$\sum_{i=1}^{nc}\frac{z_i(K_i-1)}{1+F_{\mathrm{V}}(K_i-1)}=0 \tag{18}$$

where z_i is the total mole fraction of component i in both phases; F_{V} is the molar fraction of vapor phase. The initial value of K_i, is estimated by Wilson equation and the Newton iteration is adopted for updating K_i, which are expressed below,

$$K_{i,0}=\frac{P_{\mathrm{c}}}{P}\exp\left[5.373(1+\omega_i)\left(1-\frac{T_{\mathrm{c}}}{T}\right)\right] \tag{19}$$

$$K_{i,j+1}=K_{i,j}\frac{x_i\phi_{\mathrm{L},i}P_{\mathrm{L}}}{y_i\phi_{\mathrm{V},i}P_{\mathrm{V}}} \tag{20}$$

Unlike traditional vapor and liquid equilibrium (VLE) calculations where gas-liquid capillary pressure is usually neglected, capillary pressure in nanopores requires explicit consideration. The widely applied Young-Laplace equation (Dong et al., 2016) is adopted for capillary pressure calculation in nanopores considering adsorption effect, assuming the vapor and liquid phase as the respective non-wetting/wetting phase,

$$P_{\mathrm{cap}}=\frac{2\gamma_{\mathrm{ad}}\cos\theta}{r_{\mathrm{p}}-\delta_{\mathrm{ad}}} \tag{21}$$

$$\gamma_{\mathrm{ad}}=\frac{\gamma}{1+2\frac{\delta_{\mathrm{ad}}}{(r_{\mathrm{p}}-\delta_{\mathrm{ad}})}} \tag{22}$$

where γ and γ_{ad} is the IFT between the vapor-liquid phases in bulk and nanopores, respectively; θ refers to the contact angle between vapor-liquid interface which is set to be 30° (Sun et al., 2024). In clarification, the empirical correlations used in the construction of nano-confinement effect were summarized in Table 4, which includes the adsorption layer thickness, critical property shifts and interfacial tensions in the confined pores. The Macleod-Sugden model is generally used to calculate the IFT of multicomponent mixtures in macropores (Sobecki et al., 2020):

$$\gamma=\left(\rho_{\mathrm{L}}\sum_{i=1}^{nc}x_i\xi_i-\rho_{\mathrm{V}}\sum_{i=1}^{nc}y_i\xi_i\right)^4 \tag{23}$$

Table 4
Summary of nano-confinement effect correlations.

Effects	Correlations	Validation range	Sources
L-J fluid	$\sigma_{LJ} = 0.244\sqrt[3]{\frac{T_{cb}}{P_{cb}}}$	Component: C_1–C_7, CO_2	Tee et al. (1966)
Adsorption	$\delta_{ad} = \frac{m}{\ln(r_p/\sigma_{LJ})} + n\left(\frac{\sigma_{LJ}}{r_p}\right)$	Component: C_1–C_{10}, CO_2; r_p: 1–1000 nm	Zhang et al. (2019b)
Critical property shifts	$T_c = T_{cb}\left[1 - 0.9409\frac{\sigma_{LJ}}{r_p - \delta_{ad}} + 0.2415\left(\frac{\sigma_{LJ}}{r_p - \delta_{ad}}\right)^2\right]$	Cylindrical pore $\delta_{ad} < r_p < 1000$ nm	Zarragoicoechea and Kuz (2004)
Interfacial tension	$\gamma_{ad} = \frac{\gamma}{1 + 2\frac{\delta_{ad}}{(r_p - \delta_{ad})}}$		Tolman (1949)

where ξ_i is the parachor number of component i; ρ_V and ρ_L are the density of vapor and liquid phase, respectively.

3.4. Vanishing interfacial tension method

The VIT method is generally used to determine the MMP of shale oil-CO_2 mixtures (Cao and Gu, 2013). The IFT between vapor and liquid phase at equilibrium state was calculated by the Macleod-Sugden model based on the thermodynamic flash calculation results as mentioned above. For the shale oil-CO_2 system, the MMP is determined by extrapolating the linear regression curve of IFT versus equilibrium pressure to zero IFT.

4. Results and discussion

4.1. Model validation

The confined fluid model considering nanoconfinement effect and capillarity has demonstrated extremely high reliability in estimating the MMP of CO_2 and Bakken oil (Sun et al., 2024). However, this model has not been applied to predict the IFT and MMP of CO_2-shale oil in the Sichuan Basin. Therefore, we calculated the IFT of CO_2-shale oil using this model and CMG-Winprop to verify its feasibility. The pore radius was set at 10 μm and the vapor-liquid phase contact angle was set to 90°. As shown in Fig. 4(a), the IFT calculated by CMG-Winprop under different pressure conditions is in good agreement with that obtained by the model. Additionally, we also compared the IFTs of CO_2–C_{10} binary mixture in 100 nm pores at 326.15 K calculated using the model with the experimental results (Zhang et al., 2019a). As shown in Fig. 4(b), both the simulation results and experimental results show a strong negative correlation with pressure. The simulation results are in good agreement with the experimental results, with maximum deviation of 5.40%. This indicates the applicability of the model to calculate the IFT of binary mixtures in nanopores.

Moreover, we further calculated the MMP for a CO_2-alkanes mixture (with a molar ratio of C_6H_{14}: C_8H_{18}: $C_{12}H_{26}$: $C_{16}H_{34}$ = 0.3: 0.2: 0.2: 0.3) in different pore sizes (1000, 100 and 30 nm) at 298 K. As shown in Table 5, the measured MMP of CO_2-alkanes using nanofluidic experiments was 5.5617, 6.0124 and 6.4991 MPa in 30, 100 and 1000 nm pores, respectively (Wang Y. et al., 2024). The calculated MMP using the confined fluid model for different pore sizes shows good agreement with the nanofluidic results, yielding an error of 10.02%–14.17%. Despite the relative errors were higher than 5%, the discrepancies between the experimental results and calculated values were within reasonable limits. Particularly, when the nanochannel scale decreases, the error is slightly greater.

4.2. Effect of critical shift and capillary pressure on phase behavior and IFT

The variations of vapor-liquid capillary pressure and interfacial tension with contact angle and pore size are presented in Fig. 5. The compositions and thermodynamic properties of shale oil components were obtained from the fitting results as shown in Tables 2 and 3, which is later used in the subsequent investigations. It can be seen that the capillary pressure is impacted

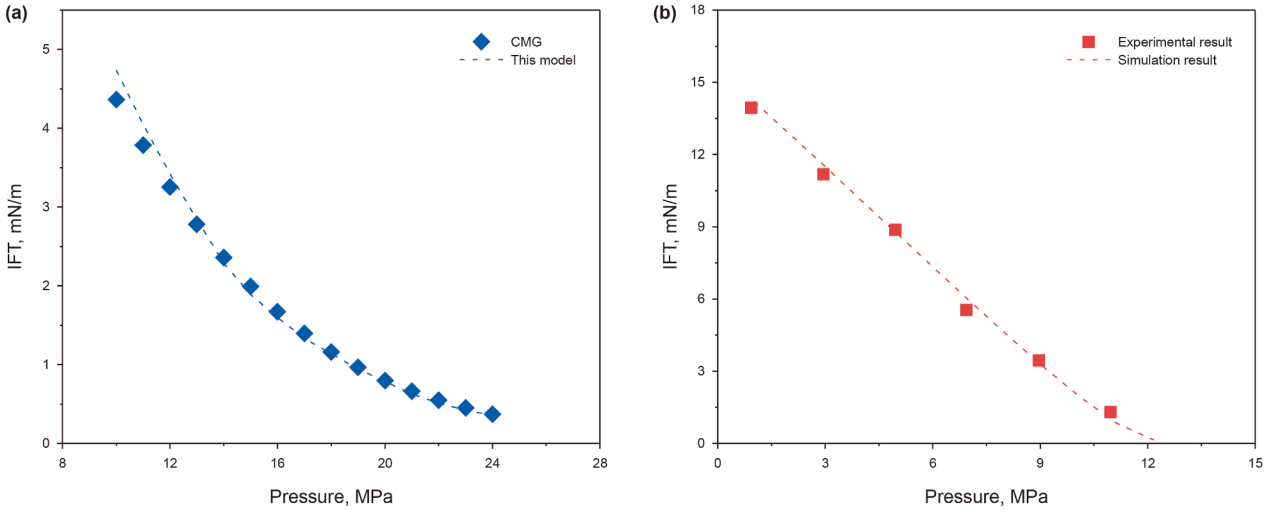

Fig. 4. Model validation via comparisons with simulation by CMG (**a**) and experimental results (**b**).

Table 5
Measured and calculated MMP for CO_2-alkanes at 298 K.

Nanochannel, nm	Experiment MMP, MPa	Calculated MMP, MPa	Relative error, %
30	5.5617	6.35	14.17
100	6.0124	6.82	13.43
1000	6.4991	7.15	10.02

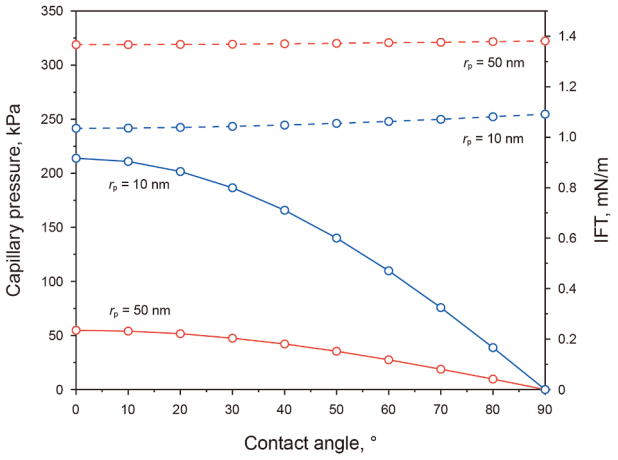

Fig. 5. Dependence of capillary pressure and IFT on surface wettability at different pore sizes.

by the nanoconfinement effect as that of 10 nm pore is largely higher than in 50 nm pore. Besides, the capillary pressure is prone to decrease with increasing contact angles, or less surface wettability of liquid phase. However, a contrary trend is exerted by the nanoconfinement effect to the interfacial tensions between vapor and liquid phases. With the increase of pore size, the interfacial tension between vapor and liquid phases increases. Moreover, the variations of interfacial tensions with changing contact angle are less profound. Therefore, the contact angle was fixed at 30°, which will not be discussed repeatedly.

To investigate the nanoconfinement effect on the phase behavior and IFT of the shale oil-CO_2 system, the phase equilibrium envelope and IFT with and without considering capillary pressure and critical properties shift are presented as shown in Fig. 6. In Fig. 6(a), the bubble point pressures were suppressed by the effect of capillary pressure, while the dewpoint pressures were slightly impacted. However, it's noted that the capillary pressure considering adsorption is evaluated by the Young-Laplace equation, in which the fluid saturation is neglected and may lead to undervalued dewpoint pressure. Actually, previous researches reported that the upper dewpoint pressure decreases while the lower dewpoint pressure increases (Liu and Zhang, 2019). Therefore, the nanoconfinement effect of critical properties shift is the main driving force to the shift and shrinkage of phase equilibrium envelope. As shown in Fig. 6(b), the IFT of shale oil-CO_2 system decreases linearly at lower pressure range and gradually at higher pressure range. Both capillary pressure and critical parameter shifts can reduce the IFT of shale oil-CO_2 system. At lower pressure region (<9 MPa), the reduction in IFT for confined fluids was primarily due to capillary pressure, and critical property shifts have less effect. However, with the increased pressure, critical property shifts became the main cause for the IFT reduction than the capillary pressure, which is consistent with previous researches (Sun et al., 2024).

4.3. Shale oil-CO_2 phase behavior with nanoconfinement effect

Fig. 7 illustrates the *P-T* phase diagrams of shale oil and shale oil-CO_2 mixtures under different pore sizes. It can be seen that the enclosed area of gas-liquid two-phase region in the phase diagram contracts as pore sizes decreases. Consequently, the critical point of the phase diagram shifts towards the lower left orientation, with critical condensation pressure and temperature decreasing. At pore radius of greater than 50 nm, the contraction of phase envelope and the shift of critical point is less pronounced. This was mostly because the adsorption and critical shift effect, which leads to less active fluid molecules and effective pore radius (Zheng et al., 2021). The effect of nanoconfinement is intensified as pore radius decreases, which leads to a reduction in the bubble point pressure and lower dew pressure. As shown in Fig. 8, the bubble point pressure of multicomponent shale oil decreases with decreasing pore radius. At pore radii of 5 nm, the bubble point pressure decreased by 23.7% from in the bulk phase. Reduction in bubble point pressure indicates longer oil phase production period and late breakthrough of dissolved gas. The *P-T* phase envelope of shale oil-CO_2 mixtures exhibits a larger two-phase region area, higher critical pressure and lower critical temperature, higher

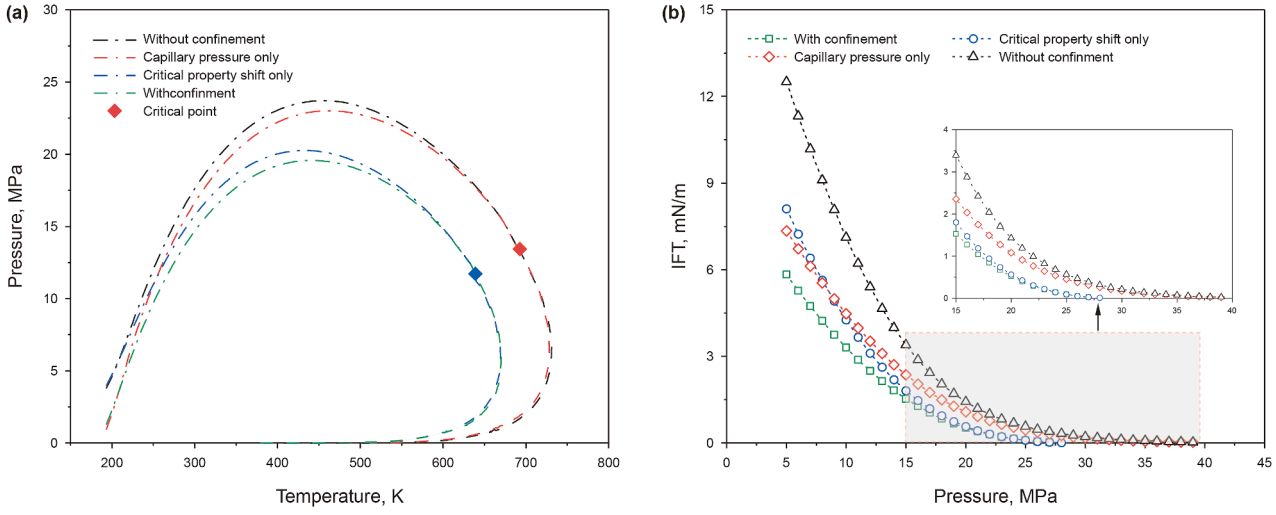

Fig. 6. Effect of critical shifts and capillary pressure on phase behavior (**a**) and IFT (**b**) in 10 nm pore at 340.15 K.

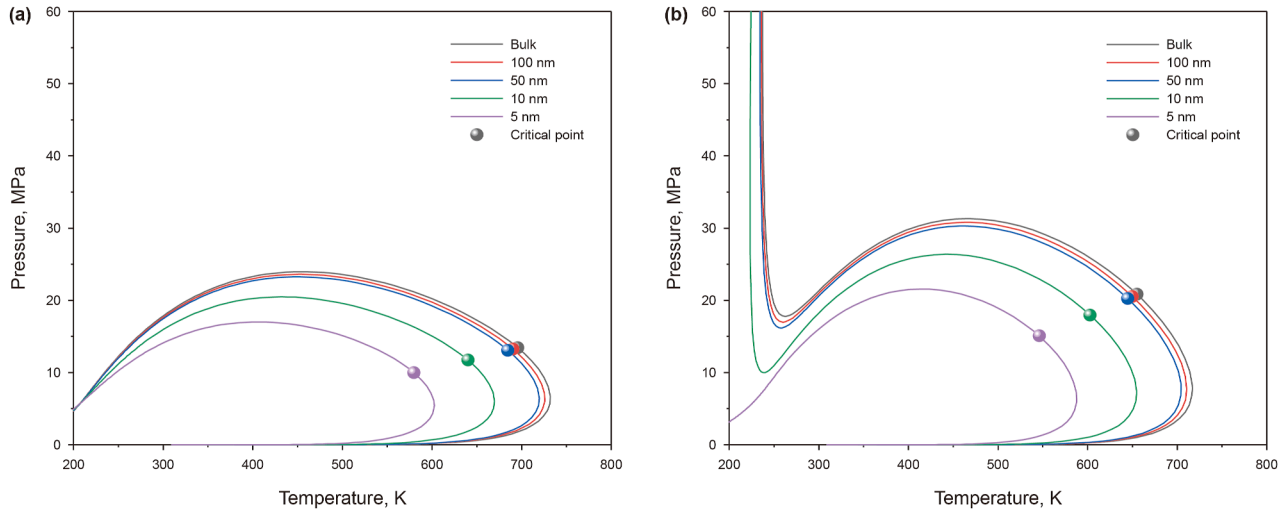

Fig. 7. *P-T* phase envelope of shale oil (**a**) and shale oil-CO_2 mixtures (**b**) in different pore sizes.

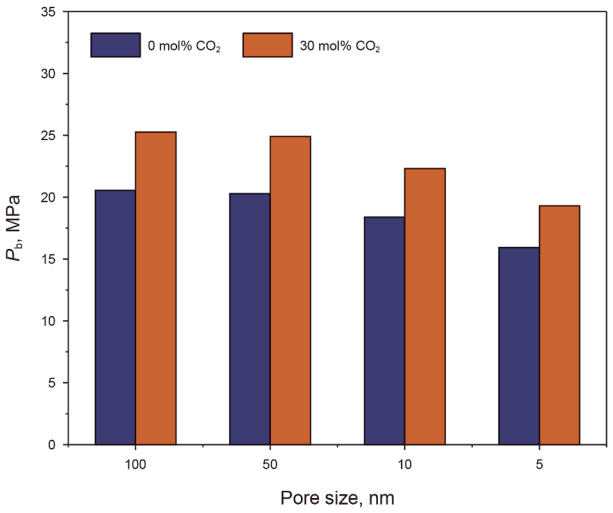

Fig. 8. Effect of pore size on bubble point pressure of reservoir fluids.

bubble point and dew point pressures compared with the shale oil. This is because the injection of CO_2 reduces the fractions of heavy components, which enables the fluids to shift towards gas-like fluids under lower pressure and temperatures. Similarly, the bubble point pressure of shale oil-CO_2 mixtures reduces as pore radius decreases.

The critical temperature and critical pressure of C_{4+}, C_{7+}, C_{13+} and C_{22+} were calculated using the modified fluid model and the results were shown in Fig. 9. As the pore size decreases, both the critical temperature and critical pressure of all the shale oil components decrease slightly and then reduces sharply. As shown in Fig. 9(a), when the pore size is less than 20 nm, the reduction of critical temperatures for C_{22+} became profound. However, the distinct decreasing tendency for other fluid components was presented with the decreased pore size (roughly 10–15 nm). This is because the molecular configuration of longer carbon chains in hydrocarbons is prone to be confined in small space and more susceptible to confinement effect. Besides, the decrease in critical pressure (Fig. 9(b)) is less evident than that of the critical temperature, indicating that critical temperature is more sensitive to pore sizes.

Fig. 10 illustrates the phase diagrams of shale oil at different CO_2 concentrations in bulk and 10 nm pore. Due to the high content of heavy components (46.65% of C_{7+}) in shale oil and comparable content of C_1 (40.84%), the phase envelope of shale oil is located between the saturation pressure line of C_1 and C_{7+}. As the CO_2 fraction increases, the two-region area expands, with the critical point moving towards the upper left of the phase envelope. This indicates that the two-phase coexisting area widens due to the solubility of CO_2 in shale oil. When CO_2 mole fraction exceeds 30%, the fluids gradually exhibit the characteristics of a condensate gas. Fig. 11 shows the changes of bubble point pressure and swelling factor with increasing CO_2 fractions. As the CO_2 fraction increases, the bubble point pressure of shale oil gradually increases. The solubility of CO_2 in light components reduces the solubility of heavy components in shale oil, leading to the precipitation and deposition of them. Thus, the bubble point pressure of the shale oil increases after CO_2 injection. Moreover, the increase of bubble point pressure is more pronounced in bulk than in nanopores. With the injection of CO_2, the volume of shale oil is expanded due to CO_2 solubility. Conversely, the swelling factor increases as the pore radius decreases.

The fluid distribution and properties of shale oil and shale oil-CO_2 mixtures are examined through flash calculations with the confined fluid model. The pressure in different pore radius is set to be 12 MPa to ensure a two-phase state. As shown in Fig. 12(a), the content of light components in shale oil gradually increases as the pore radius decreases. The smaller the pore radius, the higher the fraction of lighter components. It can be seen that the content of light component C_1–C_3 increases from 0.381 to 0.462, and the content of heavy component C_7–C_{12} and C_{13+} decreases from 0.326 and 0.226 to 0.283 and 0.196, respectively, as pore radii decreases to 5 nm. This is mainly because of the effect of critical parameter shift, causing heavy components with larger molecules to store within large pores (Song et al., 2024a, 2024b). Besides, it's noted that the content of intermediate component C_4–C_6 is slightly affected by the nanoconfinement scenarios. Fig. 12(b) shows the fluid distribution of shale oil-CO_2 mixtures under different pore radius. It can be seen that the mole fraction of CO_2 increases from 0.235 to 0.257 as pore radius decreases from 100 to 5 nm. This suggests that the nanoconfinement effect improves the ability of CO_2 to enter smaller pores in shale matrix, which facilitates the process of CO_2-EOR. Moreover, the content of C_1–C_3 within nanopores is higher when compared to the bulk region. It is noting that

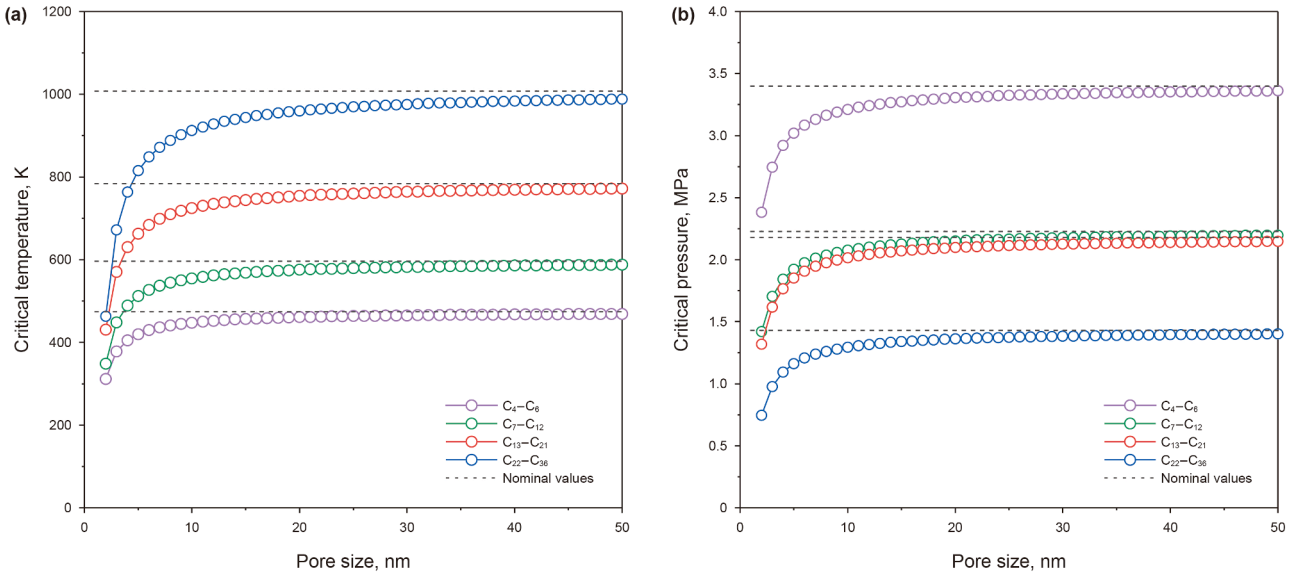

Fig. 9. Effect of pore size on critical temperature (**a**) and critical pressure (**b**) of each component.

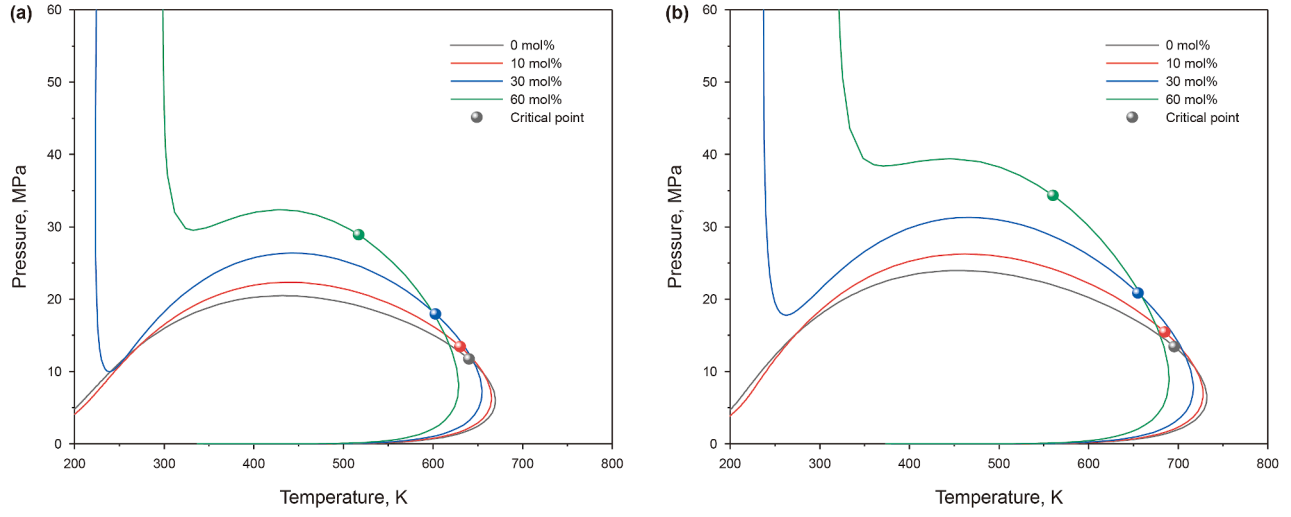

Fig. 10. *P-T* phase envelope of shale oil-CO_2 mixtures in bulk (**a**) and 10 nm pore (**b**) at different CO_2 fractions.

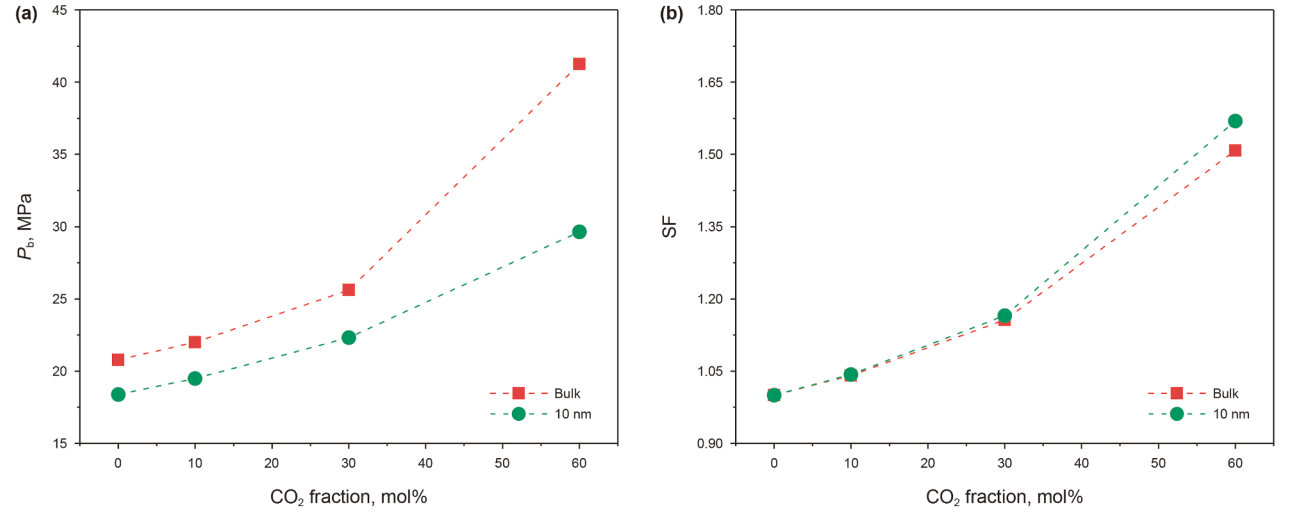

Fig. 11. Effect of CO_2 fraction on saturation pressure (**a**) and swelling factor (**b**) of shale oil-CO_2 mixtures.

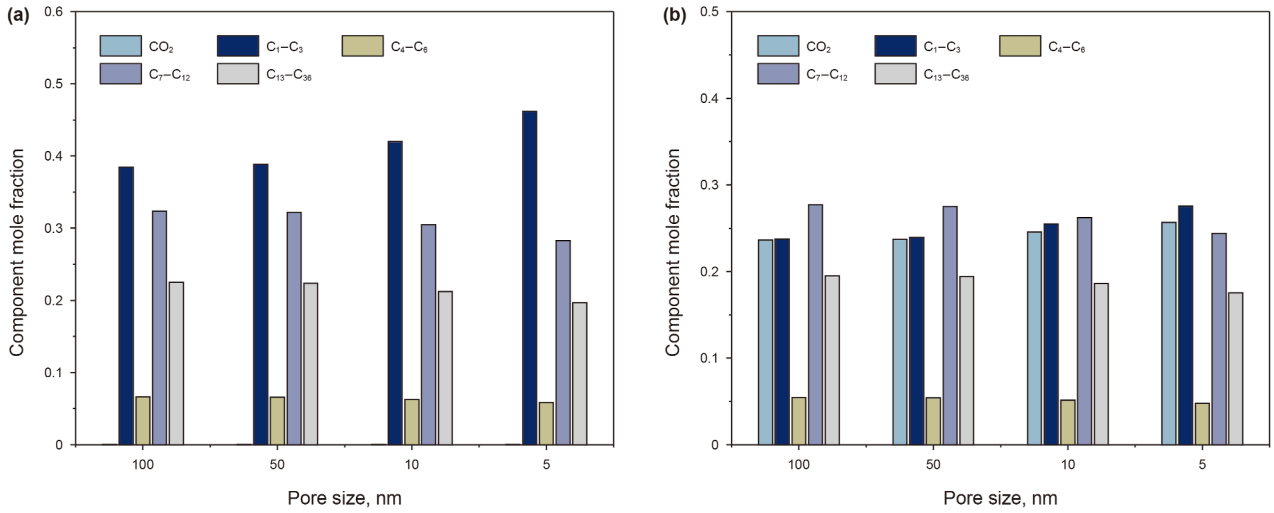

Fig. 12. Fluid distribution of shale oil (**a**) and shale oil-CO_2 mixtures (**b**) in different pore sizes.

the concentration difference between CO_2 and C_1–C_3 becomes more significant with the reduced pore size, indicating that light component C_1–C_3 is more prone to enter small pores by comparison with CO_2.

The change of fluid distribution leads to the change of fluid properties in different pore radius. As shown in Fig. 13, the density, viscosity and interfacial tension of shale oil and shale oil-CO_2 mixtures decrease as pore radius decreases. The shale oil density and viscosity decrease by 8.71% and 65.8%, respectively, as pore radii decreases to 5 nm. The IFT between gas and liquid phase reduces as the difference between the composition of gas and liquid phase is smaller in nanopores. For shale oil-CO_2 mixtures, the IFT decreases by 53.85% as pore radius reduces to 5 nm. This suggests that the nanoconfinement effect improves the miscibility of CO_2 and shale oil.

4.4. IFT and MMP of shale oil-CO_2

The MMP between CO_2 and shale oil in nanopores is a crucial factor to evaluate the viability and efficiency of miscible CO_2-EOR. In this section, we calculated the IFT between shale oil and CO_2 using the confined fluid model considering the nanoconfinement effect and determined the MMP by applying the VIT method. The effects of pore radius, temperature, injected gas type and compositions on the IFT and MMP of shale oil-CO_2 mixtures were consequently investigated.

4.4.1. Effect of pore sizes

As shown in Fig. 14(a), the IFT of shale oil-CO_2 mixtures decreases with increasing pressures. Under low pressure ranges, the IFT decreases progressively as pressure increases, which is mostly owing to the dissolution and diffusion of CO_2. However, the IFT slightly decreases under higher pressure conditions. This is because the mass transfer process at which light component of shale oil has been extracted, thus the miscibility between CO_2 and residual heavy component is difficult (Wang and Gu, 2011). In bulk condition, the MMP is estimated to be 21.6 MPa, which is consistent with the experimental MMP of 22.4 MPa obtained by slim-tube displacement method and the simulated MMP of 20.95 MPa obtained by multiple mixing-cell (MMC) method of CMG-Winprop. The IFT of shale oil-CO_2 mixtures decreases as pore radius decreases. It was reported that the effect of critical property shift is the main factor contributing to the decrease of IFT in nanopores (Sun and Li, 2021). Sun et al. (2024) calculated the IFT of CO_2-nC_6 binary mixtures with and without considering critical property shift and capillary pressure. It was concluded that the reduction of IFT of CO_2-nC_6 system in nanopores was attributed to the combined nanoconfinement effect, with the effect of critical property shift was the dominant factor. Moreover, the difference between the IFT considering different effects was marginalized when equilibrium pressure exceeds certain value. As shown in Fig. 14(b), the MMP of shale oil-CO_2 mixtures decreases by 0.47%, 9.01% and 16.31% as pore radii decreases to 50, 10 and 5 nm,

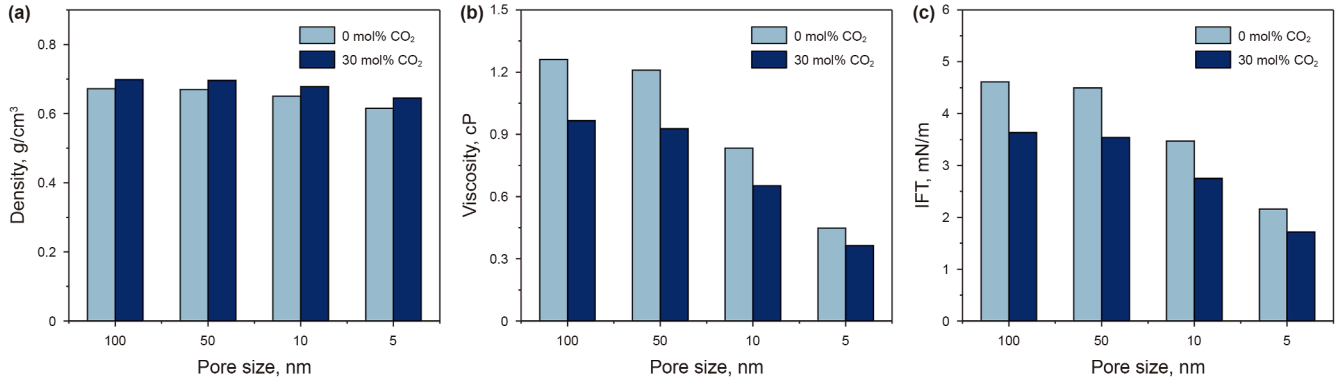

Fig. 13. Changes of oil density (**a**), viscosity (**b**), and IFT (**c**) in different pore sizes.

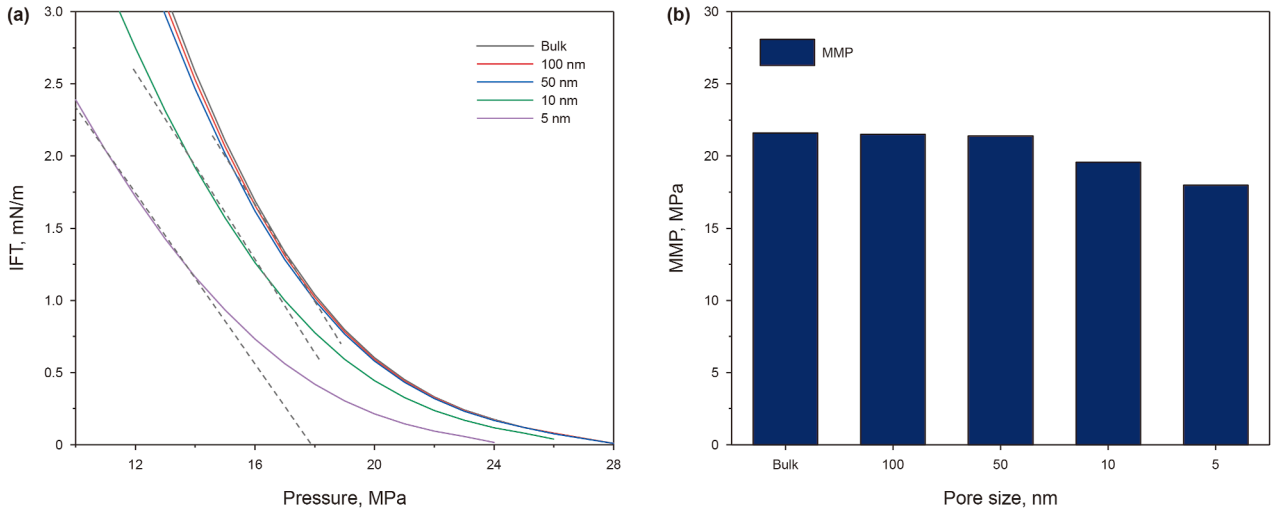

Fig. 14. Effect of pore size on IFT (**a**) and MMP (**b**) of shale oil-CO_2 mixtures.

respectively. The nanopore confinement effect on IFT and MMP is more pronounced in pore radii of less than 50 nm. It was reported that mesopores (2–50 nm) constitutes a dominant proportion of shale nanopore structures, thus the nanoconfinement effect can lower MMP in shale reservoirs and the oil production performance of shale well will be improved.

To establish the impact of pore size heterogeneity of shale oil reservoirs, the MMP of confined fluids was estimated by a mixing rule that accounts for the wide distributions of pore sizes in shale oil reservoir and averaged pore size method. The pore size distributions of two shale rocks were obtained from (Sun et al., 2024; Pang et al., 2022). The mixing rule was given as,

$$\mathrm{MMP_{mix}} = \sum_{i=1}^{Nr} D_{ri} \times \mathrm{MMP}_{ri} \tag{24}$$

where $\mathrm{MMP_{mix}}$ is the calculated MMP considering pore size distribution, D_{ri} is the proportion of pore sizes, N_r is the number of discretized pore sizes, MMP_{ri} is the estimated value at a single pore size.

The estimated results of MMP by the mixing rule and average methods were presented in Table 6. It shows that the calculated MMP by utilizing the mixing rule is slightly lower than the values calculated at single averaged pore size. The relative error is 3.2% and 4.51%, respectively. The discrepancy between the calculated MMPs increases with increasing pore size. However, it is noted that shale rocks demonstrate complex pore heterogeneity, thus incorporating the real pore size distribution into MMP estimation is important. Besides, the MMP reduction in confined fluids in shale oil reservoirs is beneficial to the CO_2 flooding or CO_2 huff-n-puff processes, which can improve gas injection efficiency and oil recovery and increase CO_2 storage.

4.4.2. Effect of temperature

Fig. 15 illustrates the IFT and MMP of shale oil-CO_2 mixtures with increasing pressure under different temperatures ranging from 313.15 to 363.15 K in 10 nm pores. It can be seen that the IFT between shale oil and CO_2 increase with temperature. This is because the solubility of CO_2 in shale oil reduces with increasing temperature under the same equilibrium pressure conditions. Lower solubility of CO_2 leads to bigger difference in oil and gas density, thus resulting in higher IFT between gas and liquid phases (Gu et al., 2013; Peng et al., 2018). However, it has also been reported that the IFT between CO_2 and crude oil decreases with temperature under lower pressure range (<6 MPa) and increases with temperature under higher pressure range (>6 MPa). At low pressure region, temperature effect is less pronounced on the IFT between CO_2 and crude oil than pressure effect because the dissolution of CO_2 is minimal. Therefore, the different thermal effect on IFT is caused by the combined influences of temperature and CO_2 dissolution.

Fig. 15(b) shows that the MMP of shale oil-CO_2 mixtures exhibits a linear relationship with temperature over the calculating range. The increase rate of MMP values for CO_2-shale oil system was 0.0645 MPa/K from the fitting curve with R^2 of 0.989, which demonstrates a good agreement between the fitted results and the calculated results. Other researchers also reported this positive linear relationship between crude oil-CO_2 MMP and temperature (Cao and Gu, 2013). Hemmati-Sarapardeh et al. (2014) determined the MMPs of CO_2 and crude oil at temperatures ranging from 313.15 to 373.15 K and obtained an increase rate of 0.1071 MPa/K. The difference between the two increase rates of MMP values may be owing to the different oil compositions. The increase of MMP with temperature was mainly attributed to the lower slope of equilibrium IFT-pressure curve at higher temperatures. Therefore, higher operating pressure is required for CO_2 and shale oil with high IFT to achieve multiple miscibility at high temperature.

In addition to temperature, the content of asphaltene was reported to have impacts on the MMP between CO_2-oil mixtures. The asphaltene molecules are mostly accumulated at the gas-liquid interfaces, thus higher content of asphaltenes leads to higher miscible pressure at the same temperature (Ghorbani et al., 2020). However, the impact of asphaltenes was not accounted for in the determination of IFT and MMP in this work. Experiments on the determination of MMP between CO_2 and two types of light crude oils conducted by (Hemmati-Sarapardeh et al., 2014) demonstrated that the asphaltenes remain stable without precipitation at any CO_2 injection pressures below MMP at asphaltene content of 13.75% and resin-to-asphaltene of around 0.97. This is because the

Table 6
MMP calculated by the mixing rule and average pore size.

Averaged pore size, nm	$\mathrm{MMP_{ave}}$, MPa	$\mathrm{MMP_{mix}}$, MPa	Relative error, %
4.35	17.39	16.85	3.20
6.12	18.52	17.72	4.51

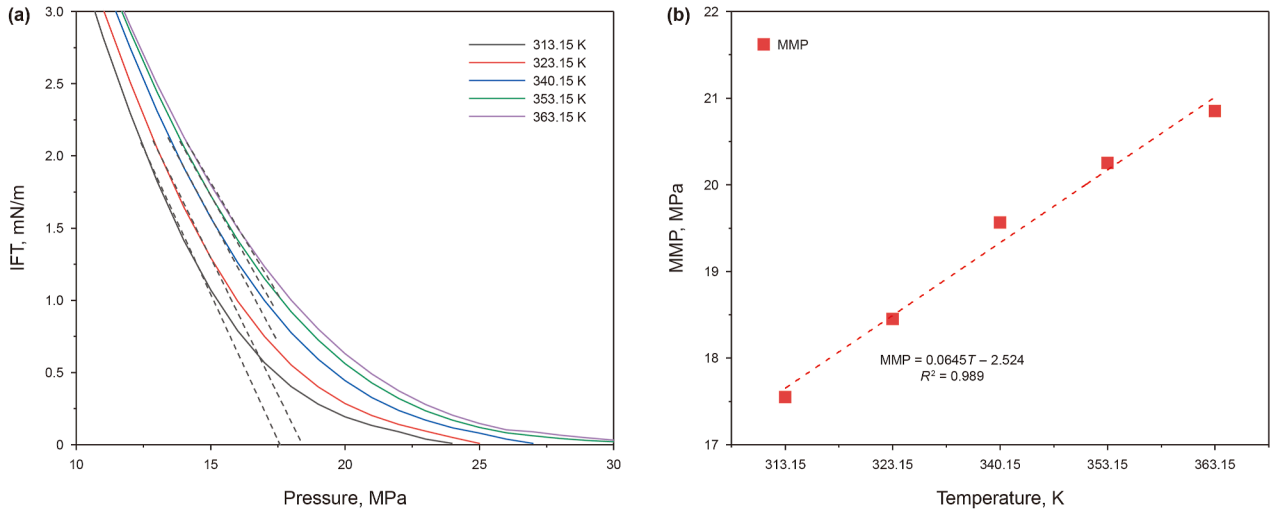

Fig. 15. Effect of temperature on IFT (**a**) and MMP (**b**) of shale oil-CO_2 mixtures.

bipolar resin molecules can surround asphaltene particles and act as bridges between the alkane components and asphaltene particles. When the resin concentration is adequate, asphaltene particles would not come together to form a segregated group because the surrounding layer is strong enough to stabilize the asphaltene particles effectively. In this study, the shale oil has the asphaltenes content of only 0.8% with resins/asphaltenes ratio of 9.75, thus the possibility of asphaltenes precipitation is less and its impact on MMP is expected to be minimal. However, the asphaltenes have different types, molecule weights and compositions (Keyvani et al., 2024), thus future research should expand to access the impact of asphaltenes and verify the universality of the model at varying conditions.

4.4.3. *Effect of injected gas*

Gas injection is one of the most recognized enhanced oil recovery methods in low-permeability shale reservoirs. In addition to CO_2, the nitrogen (N_2) and the produced gas, such as methane (CH_4), ethane (C_2H_6) and propane (C_3H_8), are generally used as injectants. It was reported that the produced hydrocarbons have good miscibility with crude oil, thus facilitating oil recovery enhancement (Hawthorne et al., 2016). Therefore, the IFT and MMP between shale oil and CO_2 and other produced hydrocarbons (C_1–C_3) were studied. As illustrated in Fig. 16(a), the IFT of all gases decreases with increasing pressure. The IFT of C_3 and shale oil is the lowest, followed by C_2, CO_2 and C_1 under the same pressure condition. This is mainly because the intermolecular forces between shale oil and C_2 and C_3 molecules are intensively higher than that between shale oil and CO_2, while C_1 molecule has a lower interaction energy with shale oil. The intermolecular forces cause the oil molecules to attract the injected gas molecules at the oil surfaces. The higher the intermolecular forces between injected gas molecules and oil molecules, the lower the IFT between two phases (Peng et al., 2018). As can be seen from Fig. 16(b), the MMP of shale oil and C_3, C_2, C_1 and CO_2 are 6.51, 10.5, 22 and 15.4 MPa, respectively.

Due to the low content of produced hydrocarbons in actual oil fields, it is possible to perform the injection of CO_2-hydrocarbon mixtures to enhance oil recovery. The IFT and MMP of CO_2-C_1 and CO_2-C_2 binary mixtures at different CO_2 fractions was calculated. It was noted that the total injected gas content was set to be 30 mol%. As can be seen from Fig. 17, the MMPs of CO_2/C_1-shale oil mixtures

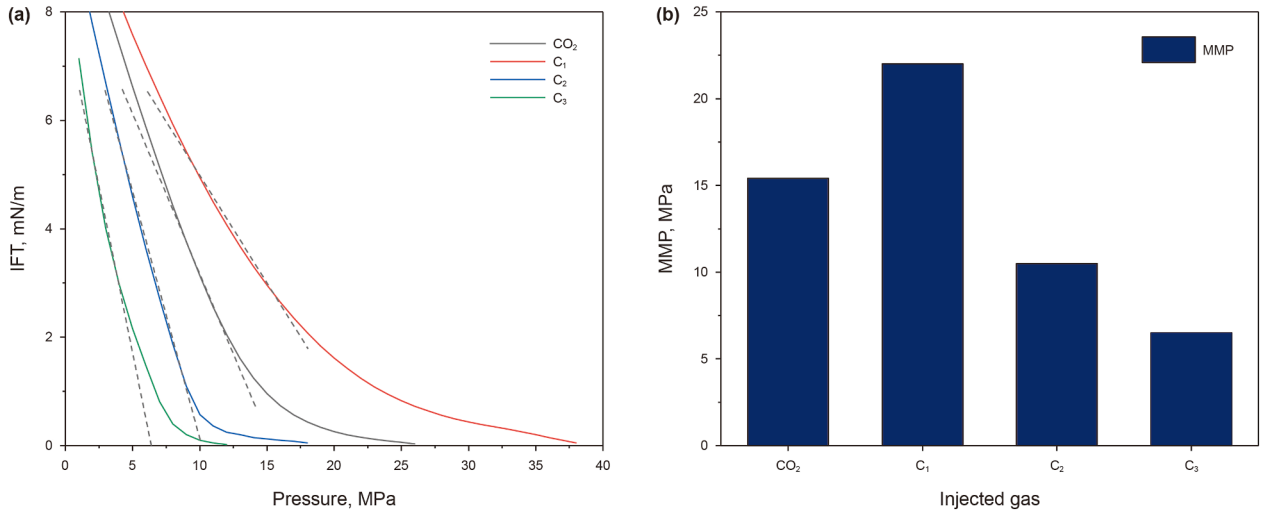

Fig. 16. Effect of injected gas type on IFT (**a**) and MMP (**b**) of shale oil.

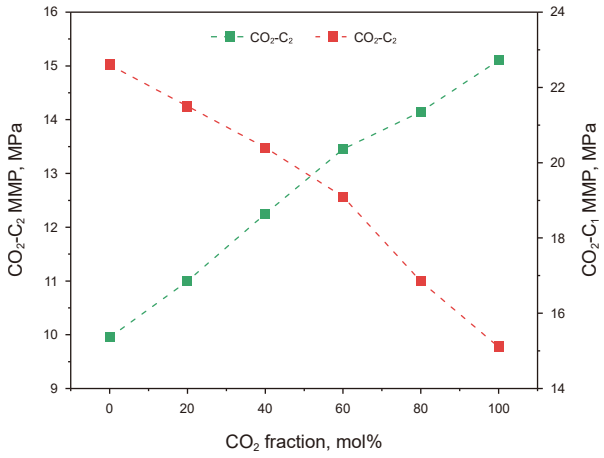

Fig. 17. Effect of CO_2 fraction on MMP of shale oil-injected gas mixtures.

decreases from 21.5 to 16.85 MPa with a reduction rate of 21.63% as CO_2 molar fraction increases from 20% to 80%. As for the CO_2/C_2-shale oil mixtures, the MMPs increase from 11 to 14.15 MPa with an increase rate of 22.26% under the same conditions. The result suggests that C_1 and C_2 has opposite effects on the MMP of CO_2-shale oil mixtures. The CO_2-shale oil MMP increases with the increase of C_1 or the decrease of C_2. In addition, the molar fraction of CO_2 has a greater effect on the MMPs of CO_2/C_2-shale oil mixtures than the MMPs of CO_2/C_1-shale oil mixtures.

5. Conclusions

Based on the PVT experiment and the theoretical confined fluid model considering the confinement effect (critical property shift and adsorption) and capillarity, the phase behavior and thermodynamic properties of shale oil-CO_2 mixtures were investigated. The effects of pore radius, temperature, injected gas type and compositions on MMP were studied. The main conclusions can be drawn:

(1) As CO_2 molar fraction increases, the shale oil volume and saturation pressure increase. The compositional fitting of PVT data between experimental and simulation results shows a good agreement, with relative error of less than 5%.
(2) As pore radius decreases, the enclosed area of gas-liquid two-phase region in the phase diagram contracts and the critical point shifts to the lower-left of the phase diagram. The nanoconfinement effect causes CO_2 and light components to enter smaller pores, thus reducing the bubble point pressure, oil density, oil viscosity and IFT of shale oil-CO_2 mixtures. The nanoconfinement effect has a pronounced influence on the phase behavior and thermodynamic property of shale oil and CO_2 mixtures.
(3) The IFT and MMP of shale oil and CO_2 mixtures decreases with decreasing pore radius. When the pore radii decrease to 50, 10 and 5 nm, the MMP of shale oil-CO_2 mixtures reduces by 0.47%, 9.01% and 16.31%, respectively. The nanoconfinement effect is more pronounced in pore radius of less than 50 nm.
(4) Temperature has a negative effect on the IFT and MMP of shale oil-CO_2 mixtures. The MMP values for CO_2-shale oil system increase by 0.0645 MPa/K from the linear fitting curve.
(5) The IFT and MMP of shale oil-C_3H_8 system is the lowest, followed by C_2H_6, CO_2 and C_1H_4 under the same testing conditions. The molar fraction of CO_2 has a greater effect on the MMPs of binary gases CO_2/C_2H_6 than those of CO_2/CH_4.

CRediT authorship contribution statement

Ying Xiong: Writing – review & editing, Writing – original draft, Resources, Funding acquisition, Conceptualization. **Peng-Fei Chen:** Validation, Investigation, Data curation, Conceptualization. **Wan-Fen Pu:** Validation, Investigation, Data curation. **Rui Jiang:** Validation, Investigation. **Qin Pang:** Writing – review & editing, Writing – original draft.

Data availability

Data is available upon request.

Conflict of interest statement

We declare that we have no financial and personal relationships with other people or organizations that can inappropriately influence our work, there is no professional or other personal interest of any nature or kind in any product, service and/or company that could be construed as influencing the position presented in, or the review of this paper.

Acknowledgments

The authors acknowledge the financial support generously provided by the National Natural Science Foundation of China (Grant No. U24A2084) and China Petroleum Southwest Oil and Gas Field Company School Enterprise Joint Research Project (Grant No. 20230302-33) for this study.

References

Adekunle, O., Hoffman, B.T., 2016. Experimental and analytical methods to determine minimum miscibility pressure (MMP) for Bakken formation crude oil. J. Pet. Sci. Eng. 146, 170–182. https://doi.org/10.1016/j.petrol.2016.04.013.
Ahmadi, K., Johns, R.T., 2011. Multiple-mixing-cell method for MMP calculations. SPE J. 16, 733–742. https://doi.org/10.2118/116823-PA.
Ashrafizadeh, S.N., Ameri Ghasrodashti, A., 2011. An investigation on the applicability of Parachor model for the prediction of MMP using five equations of state. Chem. Eng. Res. Des. 89, 690–696. https://doi.org/10.1016/j.cherd.2010.10.015.
Bao, B., Feng, J., Qiu, J., Zhao, S., 2021. Direct measurement of minimum miscibility pressure of decane and CO_2 in nanoconfined channels. ACS Omega 6, 943–953. https://doi.org/10.1021/acsomega.0c05584.
Cao, M., Gu, Y., 2013. Oil recovery mechanisms and asphaltene precipitation phenomenon in immiscible and miscible CO_2 flooding processes. Fuel 109, 157–166. https://doi.org/10.1016/j.fuel.2013.01.018.
Dong, X., Liu, H., Hou, J., Wu, K., Chen, Z., 2016. Phase equilibria of confined fluids in nanopores of tight and shale rocks considering the effect of capillary pressure and adsorption film. Ind. Eng. Chem. Res. 55, 798–811. https://doi.org/10.1021/acs.iecr.5b04276.
Ghorbani, M., Gandomkar, A., Montazeri, G., Honarvar, B., Azdarpour, A., Rezaee, M., 2020. Experimental investigation of asphaltene content effect on crude oil/CO_2 minimum miscibility pressure. Period. Polytech. - Chem. Eng. 64, 479–490. https://doi.org/10.3311/PPch.15980.
Gu, Y., Hou, P., Luo, W., 2013. Effects of four important factors on the measured minimum miscibility pressure and first-contact miscibility pressure. J. Chem. Eng. Data 58, 1361–1370. https://doi.org/10.1021/je4001137.
Hawthorne, S.B., Miller, D.J., Jin, L., Gorecki, C.D., 2016. Rapid and simple capillary-rise/vanishing interfacial tension method to determine crude oil minimum miscibility pressure: Pure and mixed CO_2, methane, and ethane. Energy Fuels 30, 6365–6372. https://doi.org/10.1021/acs.energyfuels.6b01151.
Hemmati-Sarapardeh, A., Ayatollahi, S., Ghazanfari, M.H., Masihi, M., 2014. Experimental determination of interfacial tension and miscibility of the CO_2-crude oil system; temperature, pressure, and composition effects. J. Chem. Eng. Data 59, 61–69. https://doi.org/10.1021/je400811h.
Huang, X., Zhao, Y.P., 2023. Evolution of pore structure and adsorption-desorption in oil shale formation rocks after compression. Energy 278, 127913. https://doi.org/10.1016/j.energy.2023.127913.

Iraji, B., Shadizadeh, S.R., Riazi, M., 2015. Experimental investigation of CO_2 huff and puff in a matrix-fracture system. Fuel 158, 105–112. https://doi.org/10.1016/j.fuel.2015.04.069.
Jin, Z., Zhu, R., Liang, X., Shen, Y., 2021. Several issues worthy of attention in current lacustrine shale oil exploration and development. Petrol. Explor. Dev. 48, 1471–1484. https://doi.org/10.1016/S1876-3804(21)60303-8.
Ju, Y., He, J., Chang, E., Zheng, L., 2019. Quantification of CH_4 adsorption capacity in kerogen-rich reservoir shales: An experimental investigation and molecular dynamic simulation. Energy 170, 411–422. https://doi.org/10.1016/j.energy.2018.12.087.
Keyvani, F., Safaei, A., Kazemzadeh, Y., Riazi, M., Qajar, J., 2024. Impact of nanopore confinement on phase behavior and enriched gas minimum miscibility pressure in asphaltenic tight oil reservoirs. Sci. Rep. 14, 1–18. https://doi.org/10.1038/s41598-024-64194-2.
Lee, J.H., Jeong, M.S., Lee, K.S., 2020. Comprehensive modeling of CO_2 Huff-n-Puff in asphaltene-damaged shale reservoir with aqueous solubility and nano-confinement. J. Ind. Eng. Chem. 90, 232–243. https://doi.org/10.1016/j.jiec.2020.07.016.
Li, M., Sun, M., Mohammadian, E., Ji, Y., Blach, T.P., Ostadhassan, M., Wen, J., Wu, C., Pan, Z., 2024. Confinement effect in nanopores of shale and coal reservoirs: A review on experimental characterization methods. Gas Sci. Eng. 123, 205249. https://doi.org/10.1016/j.jgsce.2024.205249.
Li, Z., Yao, J., Ren, Z., Sun, H., Zhang, L., Yang, Y., Fan, J., Kou, J., 2019. Accumulation behaviors of methane in the aqueous environment with organic matters. Fuel 236, 836–842. https://doi.org/10.1016/j.fuel.2018.09.071.
Liu, X., Zhang, D., 2019. A review of phase behavior simulation of hydrocarbons in confined space: implications for shale oil and shale gas. J. Nat. Gas Sci. Eng. 68, 102901. https://doi.org/10.1016/j.jngse.2019.102901.
Luo, S., Lutkenhaus, J.L., Nasrabadi, H., 2016. Confinement-induced supercriticality and phase equilibria of hydrocarbons in nanopores. Langmuir 32, 11506–11513. https://doi.org/10.1021/acs.langmuir.6b03177.
Nguyen, P., Mohaddes, D., Riordon, J., Fadaei, H., Lele, P., Sinton, D., 2015. Fast fluorescence-based microfluidic method for measuring minimum miscibility pressure of CO_2 in crude oils. Anal. Chem. 87, 3160–3164. https://doi.org/10.1021/ac5047856.
Pang, Q., Pu, W., Tang, X., Zou, B., Li, S., Liu, R., Pang, S., 2024. Experimental investigation and simulation of W/O emulsion flow in nanofluid flood for enhanced oil recovery. Geoenergy Sci. Eng. 239, 212973. https://doi.org/10.1016/j.geoen.2024.212973.
Pang, Y., Wang, S., Yao, X., Hu, X., Chen, S., 2022. Evaluation of gas adsorption in nanoporous shale by simplified local density model integrated with pore structure and pore size distribution. Langmuir 38, 3641–3655. https://doi.org/10.1021/acs.langmuir.1c02408.
Peng, F., Wang, R., Guo, Z., Feng, G., 2018. Molecular dynamics simulation to estimate minimum miscibility pressure for oil with pure and impure CO_2. J. Phys. Commun. 2, 115028. https://doi.org/10.1088/2399-6528/aaf090.
Pitakbunkate, T., Balbuena, P.B., Moridis, G.J., Blasingame, T.A., 2016. Effect of confinement on pressure/volume/temperature properties of hydrocarbons in shale reservoirs. SPE J. 21, 621–634. https://doi.org/10.2118/170685-PA.
Rao, D.N., 1997. A new technique of vanishing interfacial tension for miscibility determination. Fluid Phase Equilib. 139, 311–324. https://doi.org/10.1016/s0378-3812(97)00180-5.
Seyyedsar, S.M., Farzaneh, S.A., Sohrabi, M., 2016. Experimental investigation of tertiary CO_2 injection for enhanced heavy oil recovery. J. Nat. Gas Sci. Eng. 34, 1205–1214. https://doi.org/10.1016/j.jngse.2016.08.020.
Shen, Z., Sheng, J.J., 2018. Experimental and numerical study of permeability reduction caused by asphaltene precipitation and deposition during CO_2 huff and puff injection in Eagle Ford shale. Fuel 211, 432–445. https://doi.org/10.1016/j.fuel.2017.09.047.
Shi, J., Tao, L., Guo, Y., He, X., Li, Y., Bao, B., 2024. Visualization of CO_2-oil vanishing interface to determine minimum miscibility pressure using microfluidics. Fuel 362, 130876. https://doi.org/10.1016/j.fuel.2024.130876.
Sobecki, N., Wang, S., Ding, D.Y., Nieto-Draghi, C., Wu, Y.S., 2020. A multi-scale modeling of confined fluid: From nanopore to unconventional reservoir simulation. J. Pet. Sci. Eng. 193, 107364. https://doi.org/10.1016/j.petrol.2020.107364.
Song, Y., Song, Z., Chen, Z., Zhang, L., Zhang, Y., Feng, D., Wu, Z., Wu, J., 2024a. Fluid phase behavior in multi-scale shale reservoirs with nano-confinement effect. Energy 289, 130027. https://doi.org/10.1016/j.energy.2023.130027.
Song, Y., Song, Z., Meng, Y., Chen, Z., Han, X., Feng, D., 2024b. Multi-phase behavior and pore-scale flow in medium-high maturity continental shale reservoirs with oil, CO_2, and water. Chem. Eng. J. 484, 149679. https://doi.org/10.1016/j.cej.2024.149679.
Song, Z., Song, Y., Guo, J., Zhang, Z., Hou, J., 2020. Adsorption induced critical shifts of confined fluids in shale nanopores. Chem. Eng. J. 385, 123837. https://doi.org/10.1016/j.cej.2019.123837.
Sun, H., Li, H., 2021. Minimum miscibility pressure determination in confined nanopores considering pore size distribution of tight/shale formations. Fuel 286, 119450. https://doi.org/10.1016/j.fuel.2020.119450.
Sun, Q., Bhusal, A., Zhang, N., Adhikari, K., 2023. Molecular insight into minimum miscibility pressure estimation of shale oil/CO_2 in organic nanopores using CO_2 huff-n-puff. Chem. Eng. Sci. 280, 119024. https://doi.org/10.1016/j.ces.2023.119024.
Sun, Q., Zhang, N., Zhu, P., Liu, W., Guo, L., Fu, S., Bhusal, A., Wang, S., 2024. Confined fluid interfacial tension and minimum miscibility pressure prediction in shale nanopores. Fuel 364, 130949. https://doi.org/10.1016/j.fuel.2024.130949.
Tan, S.P., Qiu, X., Dejam, M., Adidharma, H., 2019. Critical point of fluid confined in nanopores: Experimental detection and measurement. J. Phys. Chem. C 123, 9824–9830. https://doi.org/10.1021/acs.jpcc.9b00299.
Tee, L.S., Gotoh, S., Stewart, W.E., 1966. Molecular parameters for normal fluids. Ind. Eng. Chem. Res. 5 (3), 363–367.
Tian, Y., Ju, B., Wang, X., Wang, H., Hu, J., Huang, Y., Liu, N., Dong, Y., 2021. Study on phase behavior of CO_2/hydrocarbons in shale reservoirs considering sieving effect and capillary pressure. Nat. Resour. Res. 30, 3533–3549. https://doi.org/10.1007/s11053-021-09886-6.
Tolman, R.C., 1949. The effect of droplet size on surface tension. J. Chem. Phys. 17, 333–337. https://doi.org/10.1063/1.1747247.
Vishnyakov, A., Piotrovskaya, E.M., Brodskaya, E.N., Votyakov, E.V., Tovbin, Y.K., 2001. Critical properties of Lennard-Jones fluids in narrow slit-shaped pores. Langmuir 17, 4451–4458. https://doi.org/10.1021/la001641a.
Wang, D., Hu, H., Wang, T., Tang, T., Li, W., Zhu, G., Chen, X., 2024. Difference between of coal and shale pore structural characters based on gas adsorption experiment and multifractal analysis. Fuel 371, 132044. https://doi.org/10.1016/j.fuel.2024.132044.
Wang, T., Tian, S., Li, G., Zhang, L., Sheng, M., Ren, W., 2021. Molecular simulation of gas adsorption in shale nanopores: A critical review. Renew. Sustain. Energy Rev. 149, 111391. https://doi.org/10.1016/j.rser.2021.111391.
Wang, X., Gu, Y., 2011. Oil recovery and permeability reduction of a tight sandstone reservoir in immiscible and miscible CO_2 flooding processes. Ind. Eng. Chem. Res. 50, 2388–2399. https://doi.org/10.1021/ie1016046.
Wang, Y., Lei, Z., Sun, L., Pan, X., Liu, Y., Xu, Z., Zheng, X., Wang, Y., Liu, P., 2024. Study on the minimum miscibility pressure and phase behavior of CO_2–shale oil in nanopores. Chem. Eng. J. 497, 154493. https://doi.org/10.1016/j.cej.2024.154493.
Wei, B., Zhong, M., Wang, L., Tang, J., Wang, D., You, J., Lu, J., 2022. Oil recovery dynamics of natural gas huff “n” puff in unconventional oil reservoirs considering the effects of nanopore confinement and its proportion: A mechanistic study. SPE Reservoir Eval. Eng. 25, 667–683. https://doi.org/10.2118/209815-PA.
Yang, Y., Liu, J., Yao, J., Kou, J., Li, Z., Wu, T., Zhang, K., Zhang, L., Sun, H., 2020. Adsorption behaviors of shale oil in kerogen slit by molecular simulation. Chem. Eng. J. 387, 124054. https://doi.org/10.1016/j.cej.2020.124054.
Zarragoicoechea, G.J., Kuz, V.A., 2004. Critical shift of a confined fluid in a nanopore. Fluid Phase Equilib. 220, 7–9. https://doi.org/10.1016/j.fluid.2004.02.014.
Zhang, K., Jia, N., Li, S., Liu, L., 2019a. Rapid determination of interfacial tensions in nanopores: Experimental nanofluidics and theoretical models. Langmuir 35, 8943–8949. https://doi.org/10.1021/acs.langmuir.9b01427.
Zhang, K., Jia, N., Liu, L., 2019b. Generalized critical shifts of confined fluids in nanopores with adsorptions. Chem. Eng. J. 372, 809–814. https://doi.org/10.1016/j.cej.2019.04.198.
Zheng, C., Liu, S., Xue, S., Jiang, B., Chen, Z., 2022. Effects of chemical solvents on coal pore structural and fractal characteristics: An experimental investigation. Fuel 327, 125246. https://doi.org/10.1016/j.fuel.2022.125246.
Zheng, Z., Di, Y., Wu, Y.S., 2021. Nanopore confinement effect on the phase behavior of CO_2/Hydrocarbons in tight oil reservoirs considering capillary pressure, fluid-wall interaction, and molecule adsorption. Geofluids, 2435930. https://doi.org/10.1155/2021/2435930.
Zhou, B., Xu, R., Jiang, P., 2016. Novel molecular simulation process design of adsorption in realistic shale kerogen spherical pores. Fuel 180, 718–726. https://doi.org/10.1016/j.fuel.2016.04.096.